



Impact of Pore Tortuosity on Electrode Kinetics in Lithium Battery Electrodes: Study in Directionally Freeze-Cast $\text{LiNi}_{0.8}\text{Co}_{0.15}\text{Al}_{0.05}\text{O}_2$ (NCA)

Benjamin Delattre,^{1,2,3,*} Ruhul Amin,^{1,4,=} Jonathan Sander,² Joël De Coninck,³ Antoni P. Tomsia,¹ and Yet-Ming Chiang^{2,z}

¹Materials Sciences Division, Lawrence Berkeley National Laboratory, Berkeley, California 94720, USA

²Department of Materials Science and Engineering, Massachusetts Institute of Technology (MIT), Cambridge, Massachusetts 02139, USA

³Laboratoire de Physique des Surfaces et Interfaces, Université de Mons, Mons 7000, Belgium

⁴Qatar Environment and Energy Research Institute, Qatar Foundation, Doha, Qatar

The prevailing electrode fabrication method for lithium-ion battery electrodes includes calendaring at high pressures to densify the electrode and promote adhesion to the metal current collector. However, this process increases the tortuosity of the pore network in the primary transport direction and imposes severe tradeoffs between electrode thickness and rate capability. With the aim of understanding the impact of pore tortuosity on electrode kinetics, and enabling cell designs with thicker electrodes and improved cost and energy density, we use here freeze-casting, a shaping technique able to produce low-tortuosity structures using ice crystals as a pore-forming agent, to fabricate $\text{LiNi}_{0.8}\text{Co}_{0.15}\text{Al}_{0.05}\text{O}_2$ (NCA) cathodes with controlled, aligned porosity. Electrode tortuosity is characterized using two complementary methods, X-ray tomography combined with thermal diffusion simulations, and electrochemical transport measurements. The results allow comparison across a wide range of microstructures, and highlight the large impact of a relatively small numerical change in tortuosity on electrode kinetics. Under galvanostatic discharge, optimized microstructures show a three- to fourfold increase in area-specific capacity compared to typical Li-ion composite electrodes. Hybrid pulse power characterization (HPPC) demonstrates improved power capability, while dynamic stress tests (DST) shows that an area-specific area capacity corresponding to 91% of the NCA galvanostatic C/10 capacity could be reached.

© The Author(s) 2018. Published by ECS. This is an open access article distributed under the terms of the Creative Commons Attribution 4.0 License (CC BY, <http://creativecommons.org/licenses/by/4.0/>), which permits unrestricted reuse of the work in any medium, provided the original work is properly cited. [DOI: 10.1149/2.1321802jes]



Manuscript submitted October 17, 2017; revised manuscript received January 15, 2018. Published February 2, 2018. This was Paper 128 presented at the National Harbor, Maryland Meeting of the Society, October 1–5, 2017.

With the ever-increasing demand for mobile applications and the growing concern for the replacement of fossil fuels, alternative energy storage has become an increasingly pressing but still unsolved problem.^{1–3} Because of their unequalled combination of high energy and power density, lightweight design and excellent lifespan, lithium-ion batteries are to date the technology of choice for portable electrochemical storage, powering applications such as electronic devices, power tools and hybrid/full electric vehicles. The prevailing electrode fabrication method for lithium-ion battery electrodes includes high pressure calendaring of electrode formulations that include active lithium materials, organic binder and conductive additives, in order to densify the electrode and promote adhesion to the metal current collector. However, this process also increases the tortuosity of the pore network in the primary transport direction. In practice, to meet operational C-rates desired, and production throughput objectives, the thicknesses of commercial electrodes are restricted to less than ~ 100 μm . Beyond this value, ion transport becomes a limiting factor and the accessible specific capacity starts to drop dramatically.⁴ With the aim of increasing cell energy density and decreasing cost by building thicker electrodes, several strategies to reduce pore tortuosity by aligning the porosity in the direction normal to the current collector have been proposed. Bae et al.⁵ demonstrated through modeling and experiments that a dual-scale porosity, partitioned between a fine-scale porous matrix and low tortuosity channels of larger scale, can greatly improve electrode kinetics while being amenable to powder-based processing. Using co-extrusion as a fabrication method, they demonstrated LiCoO_2 electrodes with three-fold higher area-specific capacity than optimized conventional electrodes tested at the same galvanostatic C-rate. Wood and Ebner⁶ described a magnetic alignment approach, later also reported by Billaud et al.⁷ in which graphite flakes functionalized with Fe_3O_4 nanoparticles were aligned in a magnetic field. Compared to a reference electrode with an isotropic porosity,

the oriented electrodes showed a three-fold improvement of their specific capacity when cycled at 1C in a lithium half-cell configuration. Sander et al.⁸ used a different magnetic field alignment approach in which sacrificial pore-forming phases rather than the active material was aligned. Using magnetically decorated microrods or liquid emulsion droplets of a ferrofluid phase, they produced anisotropic, low-tortuosity microstructures in LiCoO_2 which demonstrated more than twice the area capacity of a reference sintered electrode with the same porosity, in model electric vehicle drive cycles.

In this work, freeze-casting was used to produce porous $\text{LiNi}_{0.8}\text{Co}_{0.15}\text{Al}_{0.05}\text{O}_2$ (NCA) cathodes with an interconnected, highly aligned microstructure. The pore structure was systematically varied in order to investigate quantitatively the relationship between pore tortuosity and electrode kinetics. Freeze-casting is a recently-developed shaping technique able to produce low-tortuosity structures by using ice crystals as a pore-forming agent. The technique is based on the unidirectional freezing of a typically water-based particle suspension. As the suspension undergoes directional freezing, acicular ice crystals grow, repelling and entrapping the suspended particles between the growing ice crystals, generating an anisotropic structure. Multiple processing strategies, including modifying the freezing vehicle⁹ or using processing additives,^{10,11} can be used to further manipulate the ice crystal morphology while keeping precise control over the net porosity. After removing the ice by sublimation, samples may be used as-is or further consolidated by sintering. This versatile technique has been successfully applied to a wide range of applications, including gas separation devices,¹² scaffolds for tissue engineering,^{13–16} solid oxide fuel cells electrodes,^{17,18} composite materials,^{19,20} and others.⁹

In lithium-ion cells, transport kinetics at either the positive or negative electrode may be performance-limiting, depending on specific electrode characteristics and the mode of use. For example, during charging, the limitation is most often at the graphite negative electrode, where insufficiently fast lithium uptake leads to overpotentials sufficient to plate lithium metal. During discharge, either electrode may in principle be rate-limiting. For the present study, we focus on the positive electrode, recognizing that tortuosity improvements may benefit either electrode. NCA was selected here as the cathode-active

*These authors contributed equally to this work.

*Electrochemical Society Student Member.

^zE-mail: ychiang@mit.edu

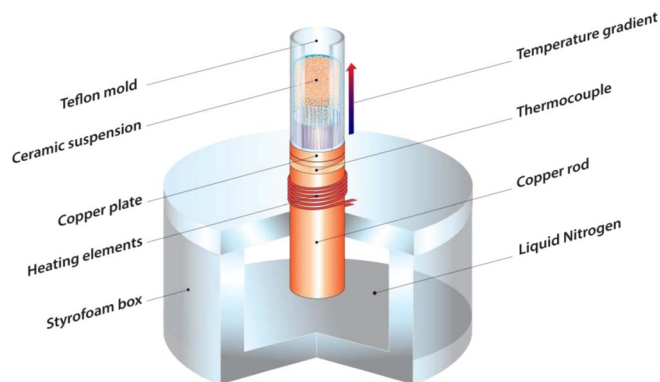


Figure 1. Scheme of a freeze-casting stage as used in the present work. Adapted from “Biomaterials by freeze casting”, by Wegst et al., 2010, Phil. Trans. R. Soc. A, 368, p. 2099–2121. Adapted with permission.

material for its overall lower cost, superior specific capacity and specific energy compared to other compounds such as LiCoO_2 (LCO), LiFePO_4 (LFP) or $\text{LiNi}_{1-x-y}\text{Mn}_x\text{Co}_y\text{O}_2$ (NMC). As we show, thick, sintered single-phase NCA electrodes can be prepared that are free of the binder and carbon conductive additives used in conventional electrodes. Freeze-cast and sintered NCA electrodes with a wide range of pore topologies have been created, and their tortuosity characterized using two complementary methods: X-ray tomography combined with thermal diffusion simulations and electrochemical transport measurements. Galvanostatic charges/discharges at various C-rates, hybrid pulse power characterization (HPPC) and dynamic stress tests (DST) were performed to evaluate the cells electrochemical performance. Compared with typical Li-ion composite electrodes, our freeze-cast electrodes showed a significant improvement in area specific capacity while preserving high power capability.

Experimental

Slurry preparation.—NCA powder ($\text{LiNi}_{0.8}\text{Co}_{0.15}\text{Al}_{0.05}\text{O}_2$, density = 4.75 g/cm^3 , $d_{50} = 5.6 \text{ }\mu\text{m}$) (NAT-1050, Toda America, Battle Creek, MI) was planetary-milled for 6 hours to decrease the averaged particle size and avoid settling during the freezing process. NCA powder, with a solids loading of 30 vol.%, was mixed with distilled water, 1 wt% of Darvan 7N (R. T. Vanderbilt Co., Norwalk, CT), 1 wt% of Poly (ethyl-glycol) (PEG-300, Sigma-Aldrich), and 2 wt% of Aquazol polymer (ISP) with a molecular weight of 50,000 g/mol. The slurry was finally ball-milled for 20 h.

Freeze-casting.—The custom-made freezing stage (Figure 1), whose characteristics are reported in a previous work (see Figure 1) was used, composed of a liquid nitrogen tank, a copper rod equipped with a ring heater and a cylindrical Teflon mold with a base diameter of 10 mm and a height of 20 mm. A control unit, linked to the ring heater, was used to adjust the cooling rate during the solidification process. When completely frozen, the sample was tapped out of the mold and freeze-dried for at least 48h at -50°C under 0.035 mbar vacuum (Freeze dryer 8, Labconco, Kansas City, MI).

Sintering and cutting.—All the samples were sintered in an air furnace (1216BL, CM Furnaces Inc., Bloomfield, NJ) for 1 h at 840°C . Samples were then cut into slices ($\approx 330 \text{ }\mu\text{m}$ thick) using a saw with diamond-coated wire blades. The area-specific capacity of the electrodes used for electrochemical testing is $15\text{--}16 \text{ mAh/cm}^2$, based on the C/10 discharge specific capacity of the NCA cathode.

Characterization of structural features.—The microstructure of the scaffold was analyzed using field-emission scanning electron microscopy (JSM-5700F, JEOL, Japan) at an acceleration voltage of 5 kV, without any additional conductive coating. The total porosity of

the electrodes was measured by Archimedes' method, using isopropyl alcohol as a fluid, and averaged over 3 measurements for each sample. For each electrode, structural parameters such as the pore size and the lamellae thickness were determined from SEM images by averaging 50 measurements using ImageJ.

Tortuosity measurements using polarization/depolarization.

The ionic conductivity/diffusivity of pure electrolyte solution was first calculated from the fit of $\ln |U(t) - U(t = \infty)|$ vs. time (Figure S3) and a porous electrode soaked with electrolyte solution was measured separately to obtain the electrode tortuosity by electrochemical technique using the following equation: $D_{eff} = \frac{\epsilon}{\tau} D_0$ where ϵ is the porosity, τ the tortuosity, and D_0 is the diffusivity of an ion in the electrolyte and D_{eff} is the diffusivity of ion in the porous system. Measurements were performed in the symmetric cell configuration as shown in Supplementary Figure S1 and S2 in a Swagelok-type cell. For the measurement of ionic diffusivity of pure electrolyte solution, a Teflon spacer with 12 mm diameter and 2.7 mm length was used to separate the anode from the cathode. One end of the spacer was covered with lithium foil of same diameter as the spacer (or combination of Celgard separator and lithium foil) and placed in the Swagelok-type cell and filled with electrolyte solution (containing 1 M LiPF_6 in 1:1 by mole of ethylene carbonate/diethyl carbonate (EC/DEC)). The other end of the Teflon spacer was also covered with lithium foil with same diameter (or combination of Celgard separator and lithium foil). The cell configuration in the supplementary Figure S2 was used to measure the ionic diffusivity of aligned and nonaligned pore structure of electrode materials soaked with same electrolyte solution. The soaked samples were placed inside the Teflon ring then a Celgard separator ($25 \text{ }\mu\text{m}$ thick and 50% porosity) was put on both side of the sample to block electronic conductivity. The Teflon ring protects to avoid touching the one separator to the other. The lithium foil with the same diameter of samples was put on top of Celgard separator. The measurements were performed in the Swagelok-type cell. The cells were assembled inside glove box containing less than 0.1 ppm of oxygen and water. A constant current was applied using Bio-logic SA France Model: VMP3 (Claix, France) for polarization and off for depolarization measurements. Lithium ionic diffusivity was derived from the voltage polarization to steady state (polarization process) and voltage relaxation vs time (depolarization process).

Synchrotron X-ray micro-tomography.—Synchrotron X-ray tomography experiments were carried out on beamline 8.3.2 at the Advanced Light Source (Berkeley, CA). Samples were scanned with a 34 keV monochromatic beam and imaged with a PCO-Edge CCD camera at 2560×2160 pixels resolution. A field view of 1.7 mm and a voxel size of 650 nm were obtained using a $10\times$ lens. The reconstructed grayscale image sequence was imported into ImageJ and processed with a gaussian blur filter in order to reduce the noise and a contrast enhancing filter. Finally, the image sequence was binarized.

Heat flux simulations.—Avizo software was used to visualize the 3D structure and to crop the data set to a cuboid volume of $500 \times 500 \times 500$ voxels. Avizo XLab Thermo was used to calculate the effective thermal coefficient along the direction normal to the electrode plane.

Electrochemical characterization.—The sintered electrodes were electrochemically tested in lithium half-cells (Swagelok type) with their low tortuosity direction of the porosity oriented normal to the electrode plane. Electrodes were electrically connected to stainless steel current collectors using a carbon paste. The sintered samples were polished to a thickness ranging from 300 to 330 μm . One side of the electrode was first rubbed with graphite to improve the electrical contact with the metal current collectors of the cells. The liquid electrolyte mixture contained 1 M LiPF_6 in a 1:1 by mole mixture of ethylene carbonate:diethyl carbonate (EC/DEC). A combination of Whatman glass wool separator and Celgard separator (Charlotte, NC, USA) was used to separate electrodes and avoid the shorting of the cell in case of dendrite formation due to the huge change of lithium

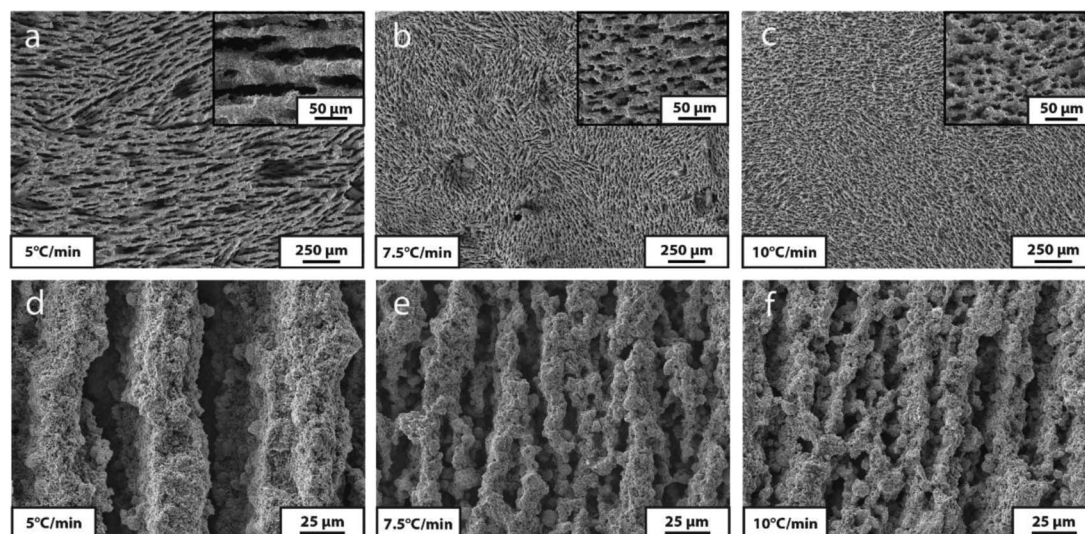


Figure 2. NCA electrode microstructures obtained from a 30 vol.% slurry with cooling rates of 5, 7.5, and 10°C/min. SEM images show the cross-sections perpendicular to (a–c) and parallel (d–f) with the freezing direction. An increase of the cooling rate shows an important change in the structure morphology which resulted in an increase of the apparent tortuosity.

thickness during charge-discharge process. A charging current equivalent from 1C to C/10 rate was applied using Bio-logic SA France Model: VMP3 (Claix, France). The current was applied at constant current constant voltage (CCCV) mode during the charge, and at constant current (CC) during the discharge.

Hybrid pulse power characterization (HPPC) was initiated with galvanostatic charging at C/5 rate followed by an open circuit hold for 1 h. A 10 s charge/10 s discharge pulse at 2C current was then applied, followed by galvanostatic discharge at 1C rate to 90% of the cell capacity (i.e., 6 min). This sequence was repeated for every 10% depth of discharge until 90% depth of discharge (DoD) was reached.

Dynamic stress test (DST) characterization was conducted with respect to the specifications determined by the USABC. The current discharge peak was here set at 2C. Supplementary Figure S7 shows the current profile of the test protocol that is repeated until the lower voltage limit of 2.5V is reached.

Results and Discussion

Water-based slurries were prepared with a solids loading of 30 vol.% $\text{LiNi}_{0.8}\text{Co}_{0.15}\text{Al}_{0.05}\text{O}_2$. In previous work,²¹ we showed that this solids loading yields a sample porosity of about 45% after sintering. Processing additives are essential to prepare suitable slurries for freeze-casting.^{10,11} A small amount of dispersant was added to distribute the particles homogeneously, and a binder was added to strengthen the green body prior to sintering. A custom-made freezing stage (Figure 1) was used to fabricate the porous structures. The process consisted of pouring the slurry in a cylindrical Teflon mold placed on top of the copper rod, which acted as a heat sink. A temperature controller linked to the ring heater and a feedback thermocouple was used to control the rate of temperature change. During the solidification process, ice crystals grew preferentially in the vertical direction, aligned with the temperature gradient, expelling and entrapping the particles between them. When completely frozen, the sample was removed from the mold and the ice phase was removed by sublimation. The sample was then sintered, and cut into slices which were polished to desired thicknesses.

Owing to the ice growth anisotropy, the freeze-cast electrodes showed a lamellar porous structure with a long-range order parallel to the freezing direction (Figure 2). Similar open architectures, with good connectivity and low tortuosity, were recently reported to have efficient ion transport and enhanced electrochemical performance.^{5,7,8} Adjusting the cooling rate allows precise control of the ice front veloc-

ity during solidification, and of the scaffold morphologies. Here, structures frozen at 5, 7.5 and 10°C/min are discussed. Figure 3 showed that an increase of the cooling rate results in an important decrease in both wall (lamella) thickness and inter-lamellar (pore) spacing. Depending on the subsequent sintering time and temperature, the micro-porosity of the walls could also be further adjusted.²¹ In addition to this size reduction, an increase of the apparent tortuosity is also observed as the cooling rate increases.

Despite playing a crucial role in transport, the tortuosity of porous materials is not trivial to measure. Indeed, to date, a multitude of approaches have been proposed in the literature, each of them being often associated with a specific definition of the tortuosity factor adapted to the field of application.²² Consequently, results can vary widely depending on the selected experimental technique and/or the calculation algorithm. Although a direct porosity-tortuosity model such as the Bruggeman correlation is sometimes used, the relation is only valid for isotropic microstructure geometry and does not take into account more complex architecture.²³ Here, two complementary approaches were used to evaluate the tortuosity of our NCA electrodes. In the first approach, the electrodes were scanned using synchrotron X-ray

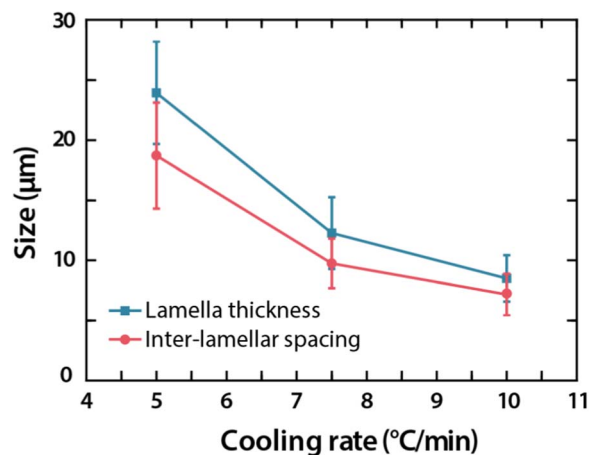


Figure 3. Average lamella (wall) thickness and inter-lamellar spacing (pore) of porous NCA electrodes freeze-casted at various cooling rates. An increase of the cooling rate resulted in a decrease of the average size of the structural parameters.

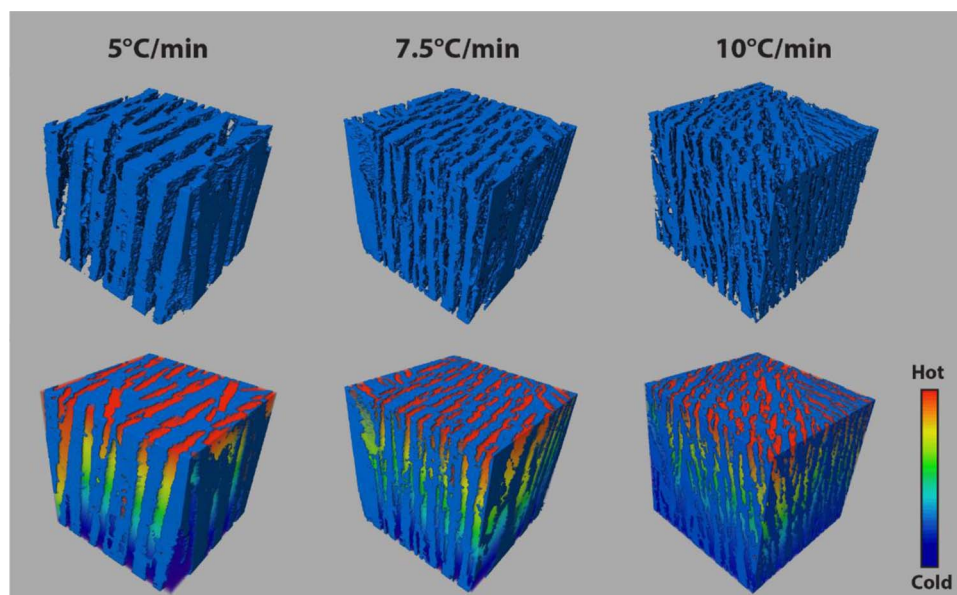


Figure 4. Top: 3D-reconstructed NCA electrodes frozen at 5, 7.5 and 10°C/min respectively. Bottom: Illustration of the temperature gradient along the direction normal to the electrode plane. The greater the local porous heterogeneity, the less uniform the temperature gradient and the more tortuous the thermal conduction pathways. The cube sides dimensions were chosen to be close to the typical experimental electrode thickness and were set to 330 μm .

micro-tomography and a heat transfer simulation based on a voxel algorithm was directly applied to the 2D binarized image sequence. Figure 4 shows the solid phase (blue) of the 3D-reconstructed electrodes frozen at 5, 7.5 and 10°C/min (top) as well as the resulting temperature gradient throughout the porous phase obtained from the heat transfer simulation. Compared to computationally-intensive fluid dynamics (CFD) simulations that require additional re-tessellation or re-meshing processes,²² the voxel based algorithm used here mimics mass transport and diffusion behavior by computing and solving Fourier's law equations directly across the voxel domain of the porous phase. This approach was recently shown to provide similar and consistent tortuosity values to other diffusion based algorithms.²⁴ Our simulations determined the effective thermal conductivity of the system, k_{eff} . The tortuosity factor τ , evaluated in the direction normal to the electrode plane, was then obtained from the following relationship:

$$\tau = V \frac{k_{bulk}}{k_{eff}} \quad [1]$$

where V is the volume fraction of the phase considered, here the electrolyte phase.

The second approach for measuring electrode tortuosity used direct current (DC) measurements of polarization and depolarization kinetics to determine the lithium ion diffusivity of the electrolyte-infused porous electrodes. The cell construction is illustrated in supplementary Figure S1 and S2; details of this technique have been discussed in previous studies.^{25,26} Figure 5a shows the time dependence of the polarization/depolarization cell voltage for the freeze-cast sample (5°C/min), with applied constant current (galvanostatic mode). The polarization/depolarization voltage ($t > T_c$), depends on time as follows:²⁷⁻²⁹

$$U_{ion} = [(i_p L) / \sigma] + \left(\frac{\sigma_{el}}{\sigma} \right) \left[\frac{i_p L}{\sigma_{ion}} \right] \left\{ 1 - (8/\pi^2) \exp \left[- \left(\frac{t}{T_c} \right) \right] \right\} \quad [2]$$

Where i_p is the applied current; L is the sample thickness; σ , σ_{el} , σ_{ion} are the total, electronic and ionic conductivities respectively and T_c is the characteristic -also called relaxation- time

Equation 2 can be expressed as:

$$\ln(U_{(t)} - U_{(t=\infty)}) = \ln(A) + \frac{8}{\pi^2} \frac{t}{T_c} \quad [3]$$

where A is a constant for a given material, $U_{(t)}$ and $U_{(t=\infty)}$ are the cell voltage at time t and $t = \infty$, respectively and where the plot of $\ln |U_{(t)} - U_{(t=\infty)}|$ vs. t generates a straight line with a slope of $T_c^{-1} \propto D_{eff}$. Polarization and depolarization voltages were thus fitted using Equation 2 to extract the effective ionic diffusivity (Figures 5b and 5c). Tortuosity factors were subsequently calculated using the following equation:

$$D_{eff} = \frac{\epsilon}{\tau} D_0 \quad [4]$$

where D_{eff} is the effective ionic diffusivity, ϵ is the porosity and D_0 , the bulk ionic diffusivity of the pure electrolyte (Figure S3). The same measurements were performed on samples solidified at 7.5 and 10°C/min., as well as on a reference sintered NCA electrode (porosity of $38 \pm 3\%$ determined by Archimede's method).

Figure 6 summarizes the tortuosity results obtained using the two techniques. Also included is the tortuosity-porosity relationship for conventional composite electrodes based on several experimental studies.³⁰ Our reference sintered NCA electrode showed a tortuosity value (3.2 ± 0.2) that is comparable to values reported in the literature for composite electrodes. From the heat transfer simulations of tomographic data, the porosity of the sintered samples was $45.4 \pm 0.8\%$ (27 measurements from 9 samples), allowing us to compare tortuosity at nearly constant porosity for a range of microstructures. All of the freeze-cast samples had tortuosity values less than ~ 2.5 . The tortuosity values obtained from the heat transfer simulations were 1.74 ± 0.09 , 1.92 ± 0.09 and 2.09 ± 0.1 , for the samples freeze-cast at 5, 7.5 and 10°C/min respectively. Figure S4 shows the statistical dispersion (at least three different samples for each cooling rate) of the tortuosity-porosity measurements.

For the DC polarization-relaxation approach, the porosity was first measured using Archimede's method and found to be $43 \pm 3\%$. The calculated tortuosity values were 1.5 ± 0.2 , 2.2 ± 0.2 and 2.5 ± 0.2 , for the samples freeze-cast at 5, 7.5 and 10°C/min respectively. Thus the two tortuosity characterization approaches yielded different absolute values of porosity, but the same systematic trend, in which an increase in the cooling rate during directional freezing resulted in an increase of the tortuosity.

Electrochemical impedance spectroscopy (EIS) measurements were then carried out on half-cells over the frequency range of 200 kHz

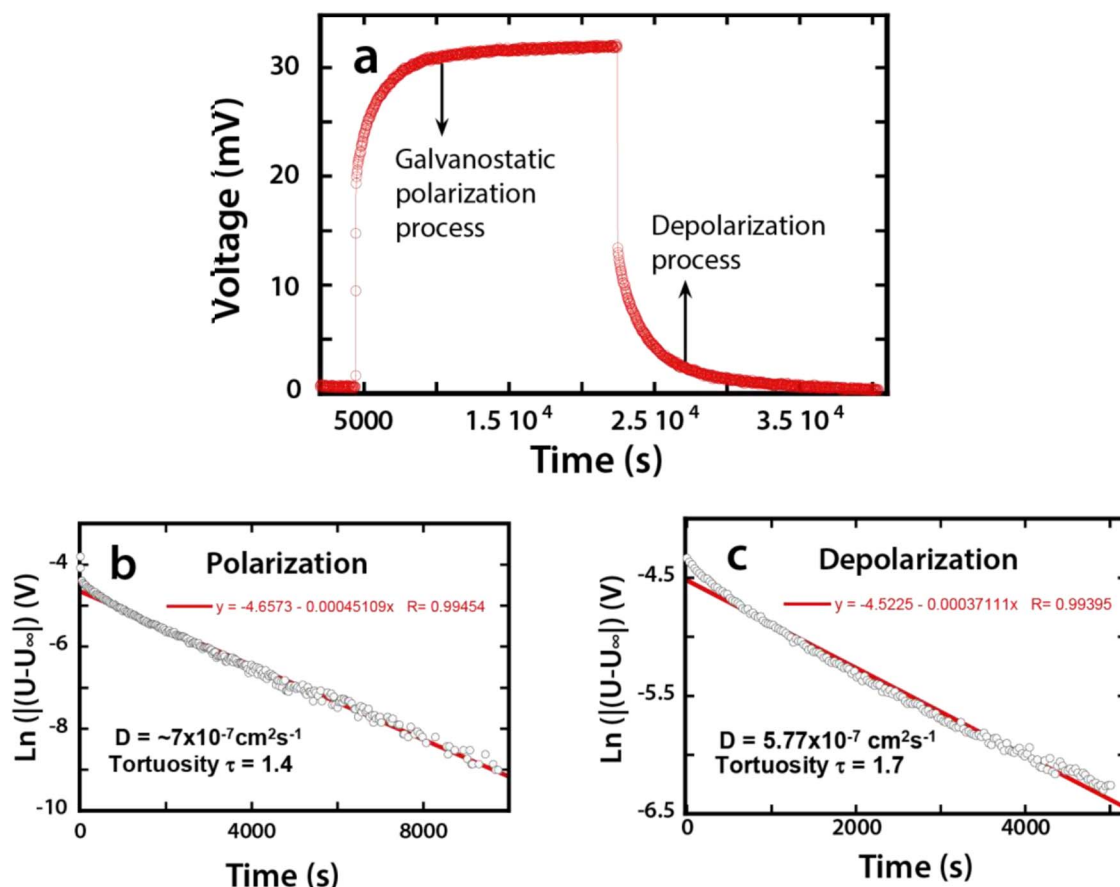


Figure 5. (a) Voltage profile of polarization-depolarization process of freeze-cast NCA (5°C/min); fit providing the diffusivity value from the (b) polarization curve and (c) depolarization curve.

to 0.05 Hz with applied AC amplitude of 10 mV. Figure 7 shows spectra for three different freeze-cast NCA electrodes, area-normalized to yield the area-specific resistance ($\Omega\text{-cm}^2$). At high frequencies, the intercepts of the Nyquist plots with the abscissa correspond to the ionic resistance of the liquid electrolyte infiltrated within the porous NCA samples, along with a minor contribution from the solid electrolyte

interface (SEI) layer. Figure 7 (inset) shows that the ionic resistance gradually increases with increasing sample cooling rate. These results are consistent with the microstructural features observed in Figures 2 and 4: the lower the cooling rate, the more directional the pore structure, suggesting lower ionic resistance. Amongst all the cells tested, no abnormally high impedance was observed in the high frequency regime, which indicates good contact between the electrodes and current collectors. In the medium frequency regime, all electrodes showed a similar semi-circle behavior corresponding to the charge transfer reaction kinetics at the electrode-electrolyte interface. The electronic resistance of the NCA electrode may also be included in this response. At lower frequency, the Warburg response observed is steeper than the expected 45° orientation relative to the abscissa. This response appears to be associated with the ionic diffusivity of electrolyte solution through the pores rather than solid state ionic diffusion.

The cells were charged under constant-current constant-voltage (CCCV) mode until the current during the constant-voltage (CV) hold reached a value lower than C/20, and discharged at constant-current (CC). Typical voltage-capacity curves during CCCV charge and C/10 discharge are shown in Figure 8a. Note that the capacity is plotted as area-specific capacity (mAh/cm^2). Using the C/10 discharge specific capacity, the low-rate area-specific capacity is calculated to be 15–16 mAh/cm^2 . Figures 8b–8d shows the discharge capacity of electrodes freeze-cast at cooling rates of 5, 7.5, and 10°C/min, respectively. Each electrode was tested under galvanostatic discharge at three C-rates (C/10, C/5, 1C). The area-specific capacities are up to a factor of four higher than the typical area-specific capacity of composite electrodes (3–4 mAh/cm^2).³¹

The sample freeze-cast at 5°C/min had the lowest measured tortuosity of the three samples (Figure 6). However, this sample exhibited

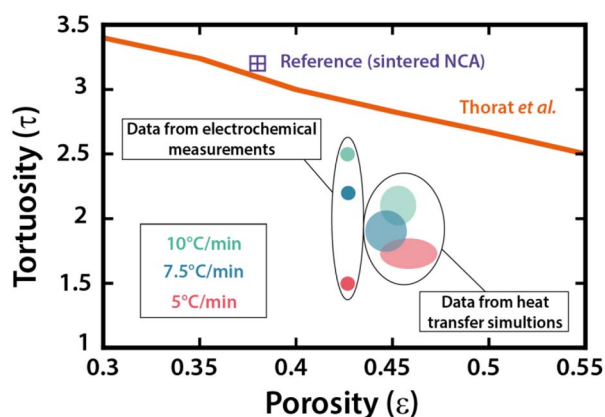


Figure 6. Tortuosity-porosity relationship for conventional and freeze-cast electrodes. Although being substantially different, the two distinct techniques provided a similar trend: an increase of the cooling rate resulted in an increase of the tortuosity. In addition, the calculated tortuosity values of the freeze-cast electrodes were significantly lower compared to the experimental data of conventional composite electrodes reported in the literature and fitted here by the relation proposed by Thorat et al.³⁰ (orange curve).

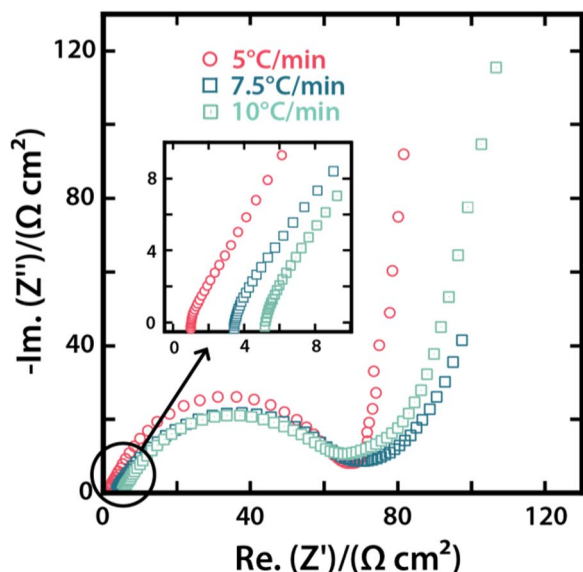


Figure 7. Impedance spectra of half-cells made using freeze-cast NCA as the positive electrode and lithium metal as the negative electrode. No significant difference in charge transfer resistances was observed among the electrodes frozen at various cooling rates whereas the ionic resistance gradually increased with the cooling rate increasing (inset).

the lowest area specific capacities, 13.3, 8.3 and 2 mAh/cm² at C/10, C/5 and 1C respectively (Figure 8b). We believe that this is due to the thicker, dense walls of the pore channels, reaching up to 30 μm in some instances, and having an average wall thickness of 24 μm (Figure S5). As analyzed below, the rate-limiting transport step may be solid-state diffusion of lithium through the densely sintered walls, rather than transport in the pore space. The sample freeze-cast at 7.5°C/min (Figure 8c), which had intermediate tortuosity amongst the three samples, realized the highest area-specific capacities, exceeding 13 mAh/cm²

at C/5–C/10, a value about four times higher than current lithium-ion electrodes.³¹ At 1C rate, over 5 mAh/cm² was obtained. The sample freeze-cast at 10°C/min (Figure 8d) exhibited area capacities over 12 mAh/cm² at low C-rates (C/5–C/10), and 4.3 mAh/cm² at 1C, significantly better than the sample freeze-cast at 5°C/min, despite having the highest tortuosity (Figure 6). The microstructure of this sample exhibited less distinct pore channels, but had the thinnest and most porous channel walls (Figures 2 and 4). These results showed that, for optimizing such anisotropic structures, not only the tortuosity but also the wall density and thickness must be considered. These trends in behavior are qualitatively consistent with the analysis of Bae et al.⁵ for electrodes with dual-scale porosity; clearly the transport at either microstructural scale may be rate-limiting.

The time scales for solid-state transport at these dimensions are consistent with the above analysis. Consider the characteristic time, t_{w24} , for lithium diffusion through a dense wall of 24 μm average thickness, corresponding to the sample freeze-cast at 5°C/min. The solid state diffusivity, D_{ss} has been determined experimentally in our previous work from measurements on 96 to 98% dense NCA monoliths.²⁶ The diffusion time scales is therefore:

$$t_{w24} = \frac{(L_{w24})^2}{D_{ss}} = \frac{(12 \cdot 10^{-4})^2}{3 \cdot 10^{-10}} = 4800 \text{ s.} \approx 1.33 \text{ h} \quad [5]$$

Here L_{w24} is the wall half-thickness. One would expect solid-state diffusion to become rate-limiting at C-rates greater than about 0.75C. Indeed, Figure 8b shows a large drop-off in capacity between C/5 and 1C. At the electrode thicknesses studied (330 μm), liquid phase diffusion remains fast enough that it should not be rate limiting. The liquid diffusion characteristic time, t_L , across a cathode of thickness L_{CT} is:

$$t_L = \frac{L_{CT}^2}{D_L} = \frac{(330 \cdot 10^{-4})^2}{2 \cdot 10^{-6}} = 544 \text{ s.} \approx 0.15 \text{ h} \quad [6]$$

This order-of-magnitude comparison indicates that liquid phase diffusion should permit maximum C-rates of ~6.6C for this electrode thickness. If the cycling rate is instead limited by solid-state diffusion, cathode wall thicknesses of 12 and 24 μm would permit maximum C-rates of about 3C and 0.75C respectively.

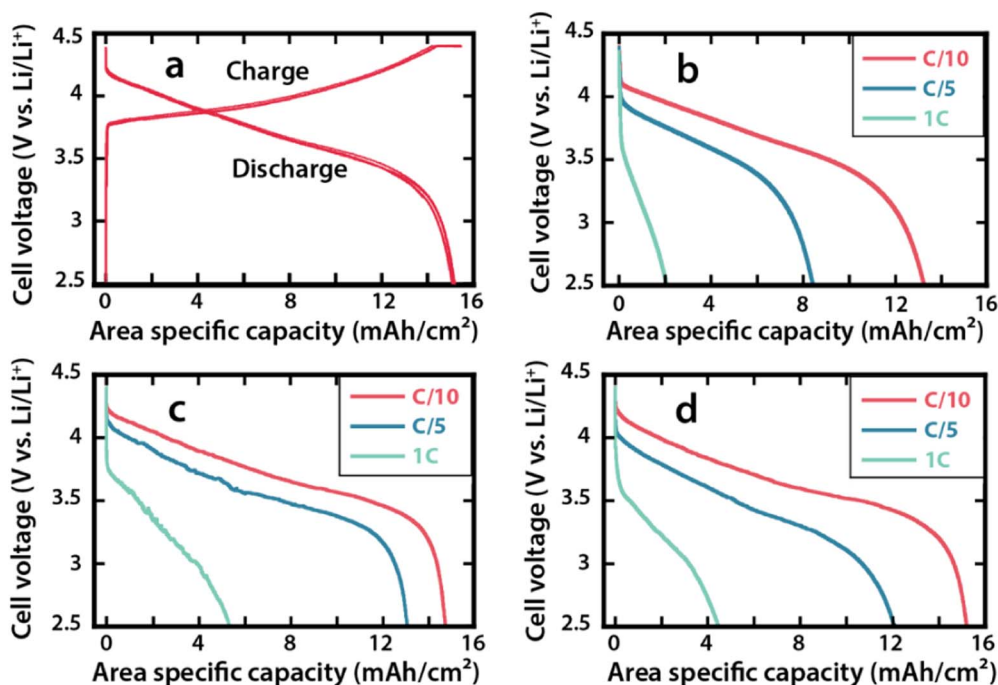


Figure 8. (a) Typical C/10 charge-discharge profile of a freeze-cast NCA electrode (thickness 330 μm, cooling rate 7.5°C/min). Continuous discharge curves of NCA electrodes freeze-casted at cooling rates of 5°C/min (b), 7.5°C/min (c), and 10°C/min (d). The capacity expressed here corresponds to the area specific capacity (mAh/cm²).

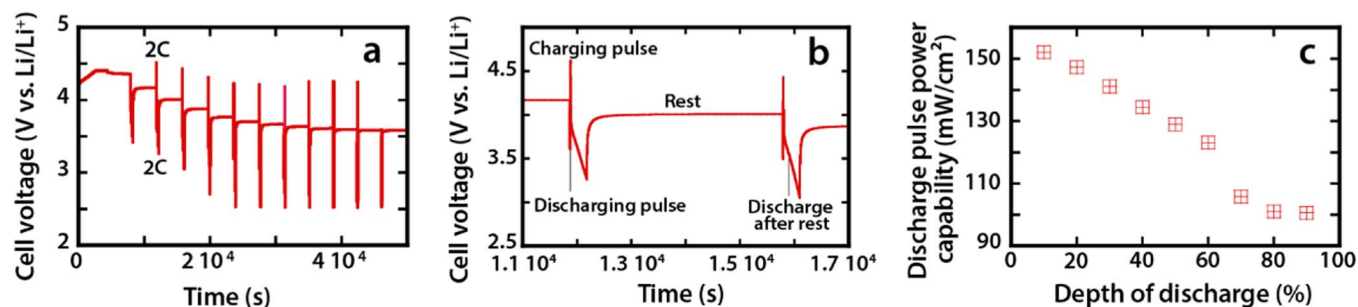


Figure 9. (a) Voltage versus time during a hybrid pulse power characterization (HPPC) test; (b) Close-up view of the sequence: a 10 s charge/10 s discharge pulse at 2C current is applied followed by galvanostatic discharge at 1C rate for 10% of the cell-capacity and a rest period; (c) area-specific discharge pulse power versus the depth of discharge for a 330 μm thick freeze-cast NCA electrode.

Overall, these results show that freezing-casting can be used to fabricate low-tortuosity thick electrodes which, when properly engineered in other aspects as well, allow for a significant increase of the specific area capacity compared with conventional composite electrodes. At C/5 rate, most of the low-rate capacity (15–16 mAh/cm^2) can be obtained. Recently, the relationship between thickness, area capacity and C-rate has been modeled and experimentally characterized for conventional composite Li-ion cathodes.³² There, measurements show that at C/5 rate, a similarly high percentage of capacity can be achieved for about one-third the low-rate capacity, 5 mAh/cm^2 . This comparison clearly demonstrates the value of low-tortuosity/aligned electrode structures.

In actual use (e.g., electric vehicles), galvanostatic cycling is rarely required; other work on aligned electrodes⁸ has shown that drive cycle requirements may be easily met by high area capacity electrodes of relatively low galvanostatic capability. To evaluate the pulse power capabilities of the present electrodes, we conducted Hybrid Pulse Power Characterization (HPPC) measurements, which incorporate 2C, 10s discharge and regenerative pulses across a range of state-of-charge.^{33,34} The NCA cathode freeze-cast at 7.5°C/min remained within the specified voltage limits throughout this test (Figure 9a). Figure 9b shows a close-up view of the voltage profile during one sequence, and the discharge power during the 2C/10s pulses are plotted as area-specific power against depth of discharge (DoD) in Figure 9c. The values ranged from 150 mW/cm^2 at low DoD to 95 mW/cm^2 at high DoD, which correspond respectively to a twofold and a four-fold factor increase compared to reference data for conventional NCA composite electrodes.³⁵ Finally, with the objective of further increasing the cell energy density, the slurry solid loading was increased to manufacture electrodes with a final total porosity of 35 vol.% after sintering (Figure S6), similar to state-of-art composite electrodes. This allowed a decrease in the electrode thickness to 160 μm while still having a high area capacity of 12.7 mAh/cm^2 . These electrodes were tested under the dynamic stress test (DST) protocol, a model drive cycle designed by the United States Advanced Battery Consortium (USABC) to simulate dynamic discharging. We discharged a fully-charged half-cell by repeatedly looping the DST test until the cell reached a lower cutoff voltage of 2.5 V (Figure S7). The specific area capacity obtained through this discharge protocol was 11.5 mAh/cm^2 (Figure 10), corresponding to 91% of the galvanostatic C/10 electrode capacity.

Conclusions

In order to evaluate the impact of engineered, low-tortuosity porosity on electrode performance, a series of additive-free, aligned-porosity, sintered NCA electrodes were fabricated by freeze-casting. The tortuosity values of the various pore morphologies were measured using the polarization/depolarization method and by thermal diffusion simulations of structure characterized by 3D tomography. Electrochemical performance of the electrodes was measured using

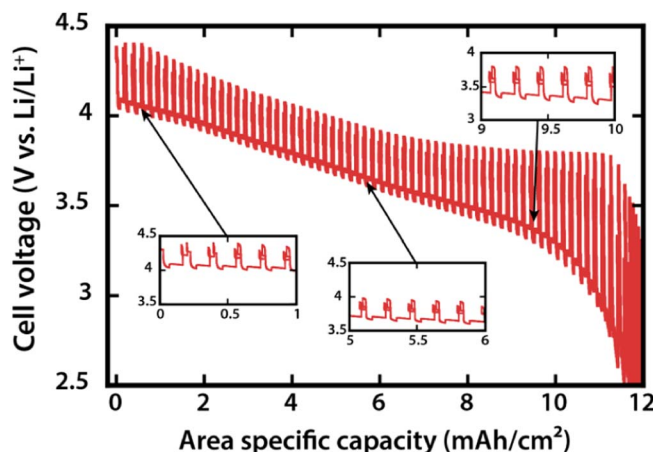


Figure 10. Discharge curve of a 160 μm thick NCA electrode freeze-cast at 7.5°C/min with a porosity of 35 vol.%. The discharge consisted of applying repeated DST cycles with 2C maximum discharge rate pulses. Under such test, the specific area capacity reached 11.5 mAh/cm^2 , which corresponds to 91% of the NCA galvanostatic C/10 capacity.

galvanostatic, HPPC, and DST protocols. Compared to conventionally processed Li-ion electrodes, a significant reduction in tortuosity factor at the same electrode porosity, exceeding a factor of 2 in the best cases, was obtained. Electrochemical testing showed that for the dual-porosity materials obtained, in which the walls of the pore channels also vary in their thickness and density, it is also important to tune the solid-state transport conditions to optimize the rate capability of the electrodes. In the best cases examined, >90% of the low-rate electrode capacity could be obtained at C/5 rate, reaching a practical area capacity of $\sim 13 \text{ mAh}/\text{cm}^2$, which is a factor of 4 higher than the typical area capacity of lithium-ion electrodes. Such electrodes also met the pulse power and drive cycle requirements embodied in the HPPC and DST test protocols.

Acknowledgments

This work was supported by the Assistant Secretary for Energy Efficiency and Renewable Energy, Office of Vehicle Technologies of the US Department of Energy under Contract no. DE-AC02-05CH11231, Subcontract no. 7056592 under the Advanced Battery Materials Research (ABMR) Program. B.D. was later supported by the Skoltech-MIT Center for Electrochemical Energy Storage. J.D.C. was supported by the Interuniversity Attraction Poles Programme (IAP 7/38 MicroMAST) of the Belgian Science Policy Office, the Région Wallone, Wallonie-Bruxelles International and the FNRS. The authors acknowledge support of the X-ray tomography beamline 8.3.2 at the Advanced Light Source (ALS) at Lawrence Berkeley National

Laboratory, which is supported by DOE's Office of Basic Energy Sciences. B.D. thanks Wallonie-Bruxelles International for a WBI World grant. The authors thank Dr. Hao Bai, Grace Lau, Dr. Sebastian Behr, James Wu and Tushar Swamy for their kind help with experiments and discussions.

ORCID

Benjamin Delattre  <https://orcid.org/0000-0002-0160-7387>

References

1. J. Ryu, Y. Park, and M. Sunwoo, *J. Power Sources*, **195**, 5735 (2010).
2. B. Kang and G. Ceder, *Nature*, **458**, 190 (2009).
3. A. Manthiram, *J. Phys. Chem. Lett.*, **2**, 176 (2011).
4. H. Zheng, J. Li, X. Song, G. Liu, and V. S. Battaglia, *Electrochim. Acta*, **71**, 258 (2012).
5. C.-J. Bae, C. K. Erdonmez, J. W. Halloran, and Y.-M. Chiang, *Adv. Mater.*, **25**, 1254 (2013).
6. V. Wood and M. O. J. Ebner, *US patent US2016/0093872 A1*, (2014).
7. J. Billaud, F. Bouville, T. Magrini, C. Villeveille, and A. R. Studart, *Nat. Energy*, **1**, 16097 (2016).
8. J. S. Sander, R. M. Erb, L. Li, A. Gurijala, and Y. M. Chiang, *Nat. Energy Nat. Energy*, **1**, 16099 (2016).
9. S. Deville, *Adv. Eng. Mater.*, **10**, 155 (2008).
10. M. M. Porter, R. Imperio, M. Wen, M. A. Meyers, and J. McKittrick, *Adv. Funct. Mater.*, **24**, 1978 (2013).
11. B. Delattre, H. Bai, R. O. Ritchie, J. De Coninck, and A. P. Tomsia, *ACS Appl. Mater. Interfaces*, **6**, 159 (2014).
12. A. Ojuva, F. Akhtar, A. P. Tomsia, and L. Bergstrom, *ACS Appl. Mater. Interfaces*, **5**, 2669 (2013).
13. Q. Fu, M. N. Rahaman, F. Dogan, and B. S. Bal, *Biomed. Mater.*, **3**, 025005 (2008).
14. S. Deville, E. Saiz, and A. P. Tomsia, *Biomaterials*, **27**, 5480 (2006).
15. H. Bai, D. Wang, B. Delattre, W. Gao, J. De Coninck, S. Li, and A. P. Tomsia, *Acta Biomater.*, **20**, 113 (2015).
16. S. Reed, G. Lau, B. Delattre, D. D. Lopez, A. P. Tomsia, and B. M. Wu, *Biofabrication*, **8** (2016).
17. S. W. Sofie, *J. Am. Ceram. Soc.*, **90**, 2024 (2007).
18. Y. Chen, J. Bunch, T. Li, Z. Mao, and F. Chen, *J. Power Sources*, **213**, 93 (2012).
19. E. Munch, M. E. Launey, D. H. Alsem, E. Saiz, A. P. Tomsia, and R. O. Ritchie, *Science*, **322**, 1516 (2008).
20. H. Bai, F. Walsh, B. Gludovatz, B. Delattre, C. Huang, Y. Chen, A. P. Tomsia, and R. O. Ritchie, *Adv. Mater.*, **28**, 50 (2016).
21. S. Behr, R. Amin, Y. Chiang, and A. Tomsia, *CFI-Ceram Forum Int.*, **92**, 39 (2015).
22. B. Tjaden, D. J. L. Brett, and P. R. Shearing, *Int. Mater. Rev.*, **1** (2016).
23. B. Tjaden, S. J. Cooper, D. J. L. Brett, D. Kramer, and P. R. Shearing, *Curr. Opin. Chem. Eng.*, **12**, 44 (2016).
24. S. J. Cooper, M. Kishimoto, F. Tariq, R. S. Bradley, A. J. Marquis, N. P. Brandon, J. A. Kilner, and P. R. Shearing, *ECS Trans.*, **57**, 2671 (2013).
25. R. Amin and Y.-M. Chiang, *J. Electrochem. Soc.*, **163**, A1512 (2016).
26. R. Amin, D. B. Ravnsbæk, and Y.-M. Chiang, *J. Electrochem. Soc.*, **162**, A1163 (2015).
27. C. Wagner, *Proc. Intern. Comm. Electrochem. Thermodyn. Kinet*, **7**, 361 (1957).
28. I. Yokota, *J. Phys. Soc. Jpn.*, **16**, 2213 (1961).
29. J. Maier, *Physical Chemistry of Ionic Materials: Ions and Electrons in Solids*, Wiley (2004).
30. I. V. Thorat, D. E. Stephenson, N. A. Zacharias, K. Zaghib, J. N. Harb, and D. R. Wheeler, *J. Power Sources*, **188**, 592 (2009).
31. W. Lu, A. Jansen, D. Dees, P. Nelson, N. R. Veselka, and G. Henriksen, *J. Power Sources*, **196**, 1537 (2011).
32. K. G. Gallagher, S. E. Trask, C. Bauer, T. Woehrle, S. F. Lux, M. Tschech, P. Lamp, B. J. Polzin, S. Ha, B. Long, Q. Wu, W. Lu, D. W. Dees, and A. N. Jansen, *J. Electrochem. Soc.*, **163**, A138 (2016).
33. S. G. Stewart, University of California, *Determination of Transport Properties and Optimization of Lithium-ion Batteries*, University of California, Berkeley (2007).
34. B. Scrosati, J. Garche, and W. Tillmetz, *Advances in Battery Technologies for Electric Vehicles*, Elsevier Science (2015).
35. J. Shim and K. A. Striebel, *J. Power Sources*, **122**, 188 (2003).